



**Vortex creation, annihilation, and nonlinear dynamics in atomic vapors**

Pierre Azam, Adam Griffin, Sergey Nazarenko, and Robin Kaiser   
*Institut de Physique de Nice, Université Côte d'Azur, CNRS, F-06108 Nice, France*

 (Received 21 June 2021; revised 17 January 2022; accepted 31 March 2022; published 14 April 2022)

We exploit techniques for generating vortices and controlling their interactions in an optical beam in a nonlinear atomic vapor. A precise control of the vortex positions allows us to observe strong interactions leading to vortex dynamics involving annihilations. With this improved controlled nonlinear system, we get closer to the pure hydrodynamic regime than in previous experiments while a wavefront sensor offers us a direct access to the fluid's density and velocity. Finally, we developed a relative phase shift method which mimics a time evolution process without changing nonlinear parameters. These observations are an important step toward the experimental implementation of a two-dimensional turbulent state.

DOI: [10.1103/PhysRevA.105.043510](https://doi.org/10.1103/PhysRevA.105.043510)

**I. INTRODUCTION**

Fluidlike properties of light in nonlinear Kerr media is an interesting and rapidly developing subject of research. In particular, they were investigated in photorefractive crystals [1,2] and thermo-optic media [3,4]. In the present paper, we will discuss light propagation in atomic vapors which was proven an effective alternative platform for fluids of light studies. In the past, this experimental platform was used to implement vortex creation [5,6], photon pre-condensation [7], and to measure the Bogoliubov dispersion relation [8,9].

There has been a vast amount of studies devoted to vortex interactions and turbulence, yet their theory is far from being complete. In the context of optical fluids, there have been significant advances in studying turbulence theoretically [10,11] and numerically [12–14]. Furthermore, with optical vortices having quantized circulations, optical turbulence is similar to turbulence in superfluids (e.g., liquid Helium) and Bose-Einstein condensates [15,16].

Optical turbulence was previously implemented in one-dimensional (1D) systems in liquid crystals [17,18] and optical fibers [19]. However, no experimental implementation of two-dimensional (2D) optical turbulence has been done so far, which is related to experimental challenges of minimizing the dissipation to nonlinearity ratio and finding optimal experimental setups in which a large number of vortices could be created and maintained in the system for a sufficiently large period of effective time so that random hydrodynamic motion of vortices could lead to universal turbulent statistics.

An interesting mechanism of vortex generation is the so-called snake instability. The snake instability of 1D solitons was first discovered in the context of 2D dispersive compressible fluids arising in plasma context [20]; it was further studied in [21] and later generalized to nonlinear defocusing media in [22]. In the context of defocusing nonlinear optics (and Bose-Einstein condensates) solitons are dark (the light intensity is less inside the soliton than in the ambient medium). In the case of optical media with saturation-type nonlinearity, such

soliton solutions were treated theoretically in [23,24]. In this context, the snake instability is known to be a precursor to generation of two-dimensional dark solitons [25] and vortex nucleation [26]. The nucleation of vortices via the snake instability [27] and their subsequent dynamics [28] have also been studied in polaritons. Dark solitons and their instability in two-dimensional condensates leading to the creation of vortices were recently studied numerically in [14,29]. In the latter paper, trains of multiple dark solitons were created in a Josephson-Junction setup where two cavities with initially unequal densities are separated by a potential barrier. This was shown to be an ideal setup for generating turbulence because the instability of multiple solitons leads to the creation of a large number of well-sustained vortices.

In the present paper, we study strongly nonlinear multiple-vortex generation of optical vortices in atomic vapors and their interactions through timelike evolution. The techniques demonstrated in this work could be scaled up to systems with large numbers of randomly moving strongly nonlinear vortices with hydrodynamic properties thereby implementing turbulent states. The strategy to achieve these results are based on a proper choice of the nonlinear parameters and the initial configuration of the incident beam, providing a robust and efficient mechanism for vortex generation. We developed a specific method precisely controlling evolution time of processes occurring in our fluid which is equivalent to the Taylor's frozen turbulence hypothesis [30], and which allows us to observe more evolved vortex creations and interactions at shorter effective times.

This work reports on experiments using the snake instability and similar mechanisms to create vortices with hydrodynamic properties. It can be viewed as a stepping stone to building future experiments on 2D optical turbulence. Initial efforts on optical vortices created as a result of the development of instability of dark soliton stripes were previously reported in atomic Rubidium experiment [6] and in photorefractive crystals [31]. The novel features exploited in the present paper include the following.

(1) In contrast to a holographic technique [4,32,33], we use a lateral shearing interferometer [34–36]: a 2D grating creates several identical replicas of the incoming wave front that interfere with each other. A real-time analysis in the Fourier space gives us access to the local intensity profile and phase gradients of the observed wave front. This lateral shearing interferometry technique has been used for studying aberrations in regimes of short wavelengths [34,35] or intense beams and in the context of adaptive optics and ophthalmology. In the context of vortices in nonlinear media, this imaging of the output field at the exit facet of the nonlinear medium allows us to accurately identify optical vortices and track their precise location without using regular interferometers requiring a reference beam, a scanning process, and a post-analysis.

(2) A better control of beam's initial conditions. Using specific geometries to optimize vortex nucleation leading to an acceleration of vortex creation process and even to controlled vortex interactions. On another hand, increasing the background beam size and shortening the nonlinear length (e.g., compared to [6]) reduces the impact of dispersion on the vortex motion. As presented in our previous study [37], we can approximate the background on which the vortices rest as flat, thereby minimizing the impact of the local refraction index fluctuations onto the vortex motions. This allows us to assume that the hydrodynamic motion of vortices is the main observed process.

## II. MODEL AND EXPERIMENTAL SETUP

The system studied here consists of a (2+1) dimension optical field propagating along  $z$  through a nonlinear medium. In the paraxial approximation, the slowly varying complex amplitude  $\psi(\mathbf{r}, z)$  of the laser field can be described by the nonlinear Schrödinger equation:

$$i \frac{\partial \psi}{\partial z} = \left( -\frac{\alpha}{2} \nabla_{\mathbf{r}}^2 - k_0 \Delta n - i \frac{\eta}{2} \right) \psi, \quad (1)$$

where  $\mathbf{r} = (x, y)$  is the coordinate in the transverse to the beam plane,  $z \approx tc$  (where  $t$  is time and  $c$  the speed of light) is the distance along the beam,  $\alpha = 1/k_0$  is the kinetic energy (dispersion) parameter,  $k_0 = 2\pi/\lambda_0$  corresponds to the wave vector of the laser beam ( $\lambda_0$  being its wavelength in vacuum), and the beam intensity is  $I = n_0 \epsilon_0 c |\psi(\mathbf{r}, z)|^2 / 2$ , with  $n_0$  being the linear index of refraction and  $\epsilon_0$  the vacuum permittivity. Further,  $\Delta n$  is the nonlinear refractive index and the parameter  $\eta$ , proportional to the inverse of the absorption length, quantifies the linear absorption rate of the medium.

In our experiment, the nonlinear refractive index is given by a saturating nonlinearity model:

$$\Delta n \propto \frac{\delta}{1 + 4\delta^2/\Gamma^2} \frac{I/I_{\text{sat}}}{1 + 4\delta^2/\Gamma^2 + I/I_{\text{sat}}}, \quad (2)$$

where  $\delta$  is the detuning between the laser and the atomic resonance with respect to the  $^{87}\text{Rb}$  D2 transition  $5S_{1/2}(F=2) - 5P_{3/2}(F=1, 2, 3)$ ,  $\Gamma = 2\pi \times 6.06$  MHz is its natural line width, and  $I_{\text{sat}}$  is the saturation intensity. For negative nonlinear refractive index ( $\Delta n < 0$ ), the medium will have a defocusing response that corresponds to an effective repulsive photon-photon interaction. Two typical lengths in the system are important: the nonlinear length scale  $z_{\text{NL}} = 1/(k_0|\Delta n|)$

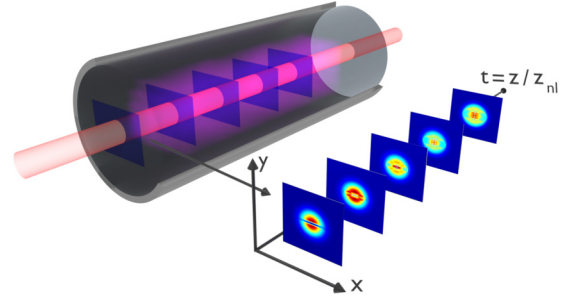


FIG. 1. Experimental scheme: Successive images show how the system evolves from the engineered initial condition after propagating along the renormalized effective time  $t \propto z/z_{\text{NL}}$ .

corresponding to the effective time scale of the propagation and the healing length  $\Lambda = \sqrt{z_{\text{NL}}/(2k_0)}$ , corresponding to the minimal length scale for density variation in the transverse plane.

Using the Madelung transformation  $\psi(\mathbf{r}, z) = \sqrt{\rho(\mathbf{r}, z)} \exp(i\phi(\mathbf{r}, z))$ , we can write a system of hydrodynamical equations for the electric field:

$$\partial_z \rho + \nabla_{\mathbf{r}} \cdot (\rho \mathbf{v}) = -\eta \rho, \quad (3)$$

$$\partial_z \mathbf{v} + (\mathbf{v} \cdot \nabla_{\mathbf{r}}) \mathbf{v} = \nabla_{\mathbf{r}} h. \quad (4)$$

This formulation describes the laser beam as a fluid of density  $\rho$  which flows at a velocity  $\mathbf{v} = \frac{1}{k_0} \nabla \phi$  in the transverse to the beam propagation plane. Here, the fluid's specific enthalpy is defined as

$$h(\rho) = \Delta n(\rho) + \frac{1}{2k_0^2} \frac{\nabla^2 \sqrt{\rho}}{\sqrt{\rho}}, \quad (5)$$

where the second term is called “quantum enthalpy” arising from quantum pressure (since this term is absent in the classical fluid equations). Our fluid of light can be characterized by the speed of sound in the medium  $c_s = \sqrt{\rho \frac{\partial(-\Delta n)}{\partial \rho}}$ .

The optical field is composed of a Gaussian background beam (with waist  $w_G = 1.1$  mm and power  $P_G = 800$  mW) overlapped with an elliptical Gaussian beam (with dimensions  $w_x = 730$   $\mu\text{m}$  and  $w_y = 140$   $\mu\text{m}$ ) having an equal central intensity as the background beam. For destructive interference (relative phase  $\varphi = \pi$ ) we obtain close to zero intensity in the middle of the elliptical beam (as in the first image on Fig. 1).

This field propagates along the  $z$  axis into a cylindrical cell of length  $L = 7$  cm and diameter 2.5 cm filled with a natural isotopic mixture of  $^{85}\text{Rb}$  and  $^{87}\text{Rb}$ . Such a vapor behaves like a nonlinear medium whose strength can be tuned experimentally. The nonlinear medium has a finite size, and reducing  $z_{\text{NL}}$  through  $\Delta n$  mimics an increase of the effective propagated time. The nonlinearity is measured using the nonlinear phase shift  $\Phi_{\text{NL}} = L/z_{\text{NL}}$ . It can be adjusted through the beam intensity  $I$ , the detuning  $\delta$ , or the atomic density of the vapor  $\rho_{\text{at}}$  (tunable with the vapor temperature) [38]. Typical experimental parameters are the background intensity  $I = 4 \times 10^5$  W/m<sup>2</sup>, the atomic density of  $\rho_{\text{at}} \approx 2 \times 10^{19}$  atoms/m<sup>3</sup> (at a temperature of  $T \approx 120$  °C), and the laser detuning scanned from  $-10$  GHz to  $-1$  GHz. The temperature measurement method is explained in the Appendix.

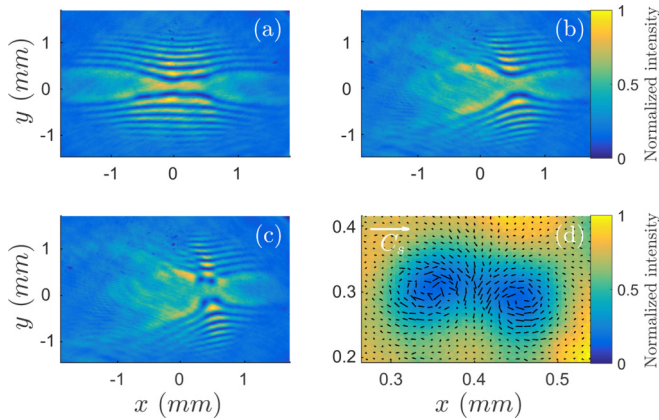


FIG. 2. Experimental observation of vortex creation by increasing the relative angle in the  $xz$  plane between beams (a)  $\theta = 0$ , (b)  $4.4 \times 10^{-4}$  rad, (c)  $5.2 \times 10^{-4}$  rad, and (d) is a zoomed vortex pair with fluid density (colormap) and velocity (vectors, normalized by  $c_s$ , shown as the white arrow).

By progressively increasing the nonlinearity using the detuning (i.e., reducing  $z_{NL}$ ), we observe the fluid evolution after different effective times at the output facet as shown in Fig. 1. A Phasics wave-front sensor captures the near field at the output of the medium ([34–36]). This offers the possibility to measure the intensity and phase of the field directly, which gives the optical fluid density and velocity in our experiment.

### III. INITIAL VELOCITY

Due to the action of the refractive index when entering the nonlinear medium, the initially elliptical dark stripe decays into a symmetric set of dark solitons on which snakelike bendings appear. Similar soliton trains appear as a result of decay of initial density discontinuities, e.g., in the Josephson junction setup [14]. As we can see Fig. 2(a), the bending pattern is concave because the initial light intensity is not strictly in one dimension: The reference beam intensity and the dark stripe depletion are larger at the beam center. Such transverse bending and amplitude modulation serve as an initial seed for the snaking instability which distorts the soliton stripes further leading to their breakup [21]. At  $\delta = -1$  GHz corresponding to  $|\Delta n| = 8.8 \times 10^{-5}$  (at the end of the nonlinear medium in the central part of the beam) the system evolves far enough to observe well-developed snake instability bendings. These parameters correspond to a nonlinear phase shift  $\Phi_{NL} = 50$ .

As shown in Fig. 2(a), in a simple configuration snake instabilities do not have the necessary evolution time to break into vortices. However, increasing the relative initial velocity between the background and the dark stripe results in an acceleration of the snake instability growth and leads to vortex nucleation. Such a relative transverse velocity can be expressed as  $v = r/t \approx \theta c$  where the angle between the background and the elliptical beam in the  $xz$  plane is approximated by  $\theta \approx r/z$  at small angles. Results of this method are presented on Figs. 2(b) and 2(c). An increase of  $\theta$  accelerates the snake instability process and allows us to observe vortex creation for the same nonlinear strength as before. The snake instability causes the soliton to break up into a pair of vortices

from  $v/c = \theta = 5.2 \times 10^{-4}$  rad. Beyond  $\theta = 8.7 \times 10^{-4}$  rad, too many fluctuations are created making the observation of snake instability decay unclear. It is possible to approximate the speed of sound as  $c_s \approx c\sqrt{\Delta n}$  which gives in our case  $c_s/c \approx 9.4 \times 10^{-3}$ . Therefore, regarding the breakup velocity  $v/c$ , an additional initial velocity between 5% and 10% of  $c_s$  is enough to observe vortex nucleation. This low (compared to speed of sound) velocity, which is necessary to reach a vortex generation regime, is a good indicator that the subsequent vortex dynamics occurs as in a nearly incompressible fluid. Figure 2(d) shows the measurement of the phase gradient (i.e., fluid's velocity) close to the vortices. The velocity circulation around each intensity minimum confirms these minima contain vortices. A snake instability always leads to breaking up into a pair of oppositely charged vortices in order to conserve the total topological charge of the system to be zero. We also observe an augmentation of the fluid's velocity between the vortices. Taking into account the residual absorption, the healing length of the medium around vortices is estimated as  $\Lambda \approx 50 \mu\text{m}$ . The core diameter of the vortices (at 0.9 of the surrounding fluid density) is around  $2\Lambda = 100 \mu\text{m}$  and the center to center distance between vortices is  $100 \mu\text{m}$ .

Detailed numerical simulations indicate that the saturation and nonlocality, which potentially could drastically reduce vortex nucleation, are negligible in our regime. Due to the geometry of our configuration, the vortices move away from each other and do not interact. Different initial conditions suitable for vortex creation need to be used in order to observe vortex interaction processes. We therefore shift the elliptical beam along the  $z$  axis (propagation axis) to give the beam a curvature when entering the medium which corresponds to an additional phase gradient (fluid velocity) over several wavelengths. In this convergent configuration (radius of curvature is around  $R = -0.5$  m), the extra velocity pushes vortices toward the center due to its specific phase gradient distribution. This specific case leads to the creation of four vortex pairs visible in Fig. 3(a). Sign of topological charges is conventionally defined depending on the winding direction as follows:  $+$  for anticlockwise and  $-$  for clockwise velocity. As in the previous case, each pair is composed of oppositely charged vortices (i.e., the topological charges of the vortices in the center of the structure are also opposite). Vortices move closer to each other (represented by arrows) due to the specific convergent configuration giving an initial velocity in this direction.

Then, they collide as shown in Fig. 3(b) and annihilate, leading to radiative loss [39]. Figures 3(c) and 3(d) highlight the emergence of this loss as sound waves visible around vortices in the Supplemental Material [40]. After the vortex annihilation, vortices form new pairs and the initial velocity disappears: After frame (d), the remaining vortices will move away from the center due to the nonhydrodynamic motion related to the overall beam expansion.

### IV. RELATIVE PHASE SCANNING

The experiment presented in Fig. 3 has been done at fixed nonlinearity and therefore at fixed effective time. The evolution depicted in this figure solely arises from a relative phase scanning between the elliptical and the background beam. Small dephasings ( $0.9\pi < \varphi < 1.1\pi$ ) were sufficient to

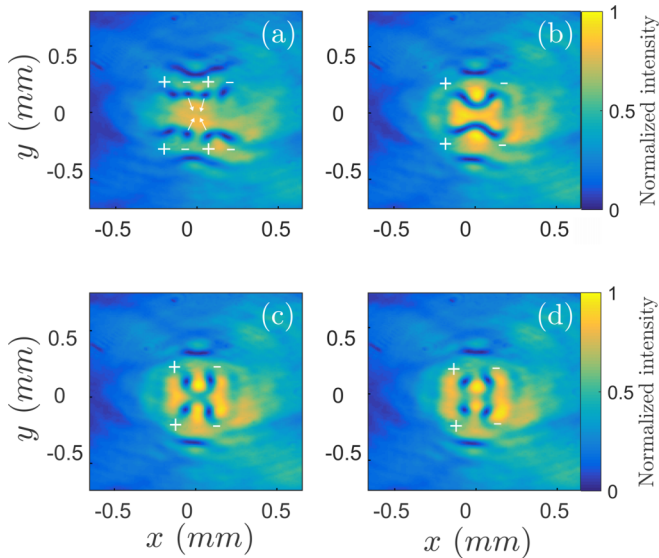


FIG. 3. Experimental observation of creation and interaction of vortices. We are using an initial convergent elliptical beam which is shifted by a phase  $\varphi$  relative to the background beam (a)–(d)  $\varphi = 0.96\pi, 1\pi, 1.05\pi, 1.10\pi$ , respectively.

observe the whole process, from the snake instabilities decaying into vortices to the vortex interactions and annihilation. An analogy can be made between this method and Taylor’s frozen turbulence hypothesis [30]. Namely, considering turbulence velocity fluctuations to be small compared to the mean flow velocity, one can approximate the time evolution of the system as its translation in the mean flow direction. In our case, scanning the relative phase changes the added velocity amplitude which remains oriented toward the center and therefore a given velocity amplitude corresponds to a specific effective time. We observe “timelike” dynamics of the instability and subsequent vortex motion and interaction by changing the relative phase between the two beams in the initial condition. The small change of phase is only timelike when the velocity of the fluid in the initial condition is parallel or antiparallel to the direction of motion of the soliton, that is, perpendicular to the long axis of the elliptical beam. For a limited range of values of the relative phase, the desired direction of the velocity is maintained with only the magnitude being altered. The subsequent timelike dynamics can be understood by considering the translational motion of a 1D soliton which can be approximated to be of the form  $f(x - v_s t)$ . In this case  $v_s$  can rescale  $t$ . As in one dimension there is no instability, this change only affects the position of the soliton. In our case the decay of the soliton is related to the transverse density variations of the background beam through which the soliton has propagated.

Figure 4 presents results of numerical simulations obtained with the converging elliptical beam as an initial condition. Upper plots correspond to a usual evolution where the system evolves in time while the lower ones are equivalent to measurements shown in Fig. 3. In addition to the good agreement between experiment and simulation when scanning the relative phase, we stress that such an agreement between

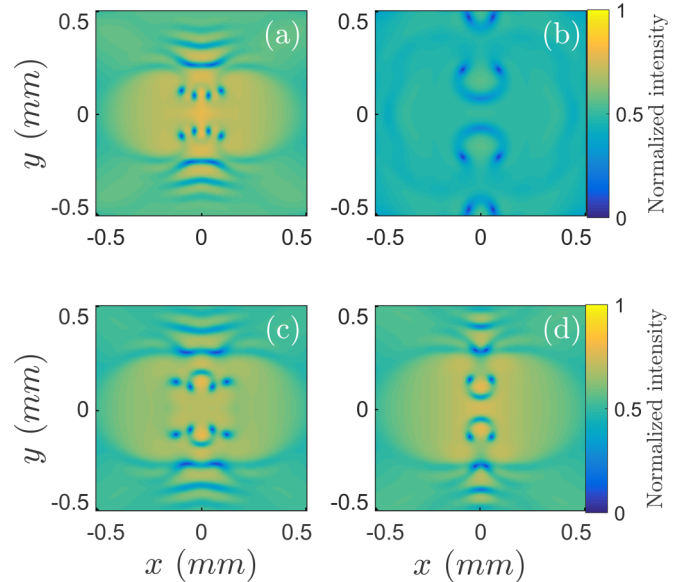


FIG. 4. Numerical simulations of the converging configuration ( $R = -0.5$  m). (a) and (b) Corresponding to a propagation along the time axis, respectively,  $z/z_{\text{NL}} = 35$  and  $z/z_{\text{NL}} = 70$  while (c) and (d) have the same effective time of propagation  $z/z_{\text{NL}} = 50$  but relative phase is, respectively,  $0.97\pi$  and  $1.05\pi$ .

the two numerical setups justifies the mapping between time evolution and phase scanning. The modification of the relative phase induces small changes in the phase gradient which can be understood as a precise tuning of the initial velocity modulus. By keeping the nonlinearity fixed (therefore the evolution time) and controlling initial velocity modulus, the system will finish its propagation at different moments of the evolution of vortices. Using the time evolution only, one needs to scan the nonlinearity from  $z/z_{\text{NL}} = 35$ – $70$  to observe the whole process while a phase scanning protocol only requires  $z/z_{\text{NL}} = 50$ . Fixing the nonlinearity during the evolution process has many advantages. In particular changing  $z/z_{\text{NL}}$  has a non-negligible impact on the beam’s dispersion.

The mean fluid density is also reduced during the time evolution while it remains constant when scanning the relative phase: This gives the possibility to study vortex dynamics with fixed  $z_{\text{NL}}$  and  $\Lambda$  during the whole process. It allows us to study effective time evolution while fixing the nonlinearity at a lower value. All these points make it a powerful tool to study vortex processes.

Finally, we have studied the diverging configuration through experiment and numerical simulations. Oppositely to the previous case, the radius of curvature is now  $R = 0.5$  m. The relative phase is scanned in the same direction as for the converging case presented in Fig. 3 (from  $\varphi < \pi$  to  $\varphi > \pi$ ). We observe in Fig. 5 that the system starts with two pairs of vortices and progressively evolves into four pairs of vortices. In fact, we are in a situation where the evolution goes in the opposite direction compared to the converging case. Considering the initial phase distribution which is opposite in these two cases, the evolution of the phase gradient (initial velocity) in each case for a same relative phase is also opposite.

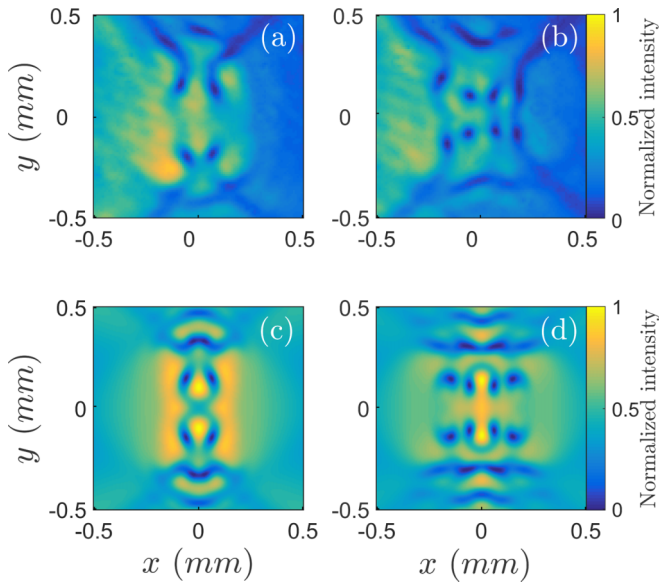


FIG. 5. Experiment (a) and (b) versus numerical simulation (c) and (d) of the diverging case  $R = 0.5$  m. Evolution is done by scanning the relative phase: (a) and (c) and (b) and (d) correspond, respectively, to  $\varphi = 0.95\pi$  and  $1.08\pi$ .

Therefore, scanning the relative phase in the same direction but in the diverging case (Fig. 5) will progressively reduce the initial velocity instead of increasing it as we saw in Fig. 3. This gives an impression of a backward process.

## V. CONCLUSIONS

Our experimental techniques have allowed us to create and observe the nonlinear dynamics and annihilation of strongly interacting vortices. The vortices were created via a snake instability of solitons arising from an initial elliptical dark stripe. The use of a wave-front sensor has greatly simplified the vortex observation and characterization by allowing us to observe the wave front *in situ*. Accelerating the dynamics allowed us to greatly reduce the needed nonlinearity. Specific initial conditions on the dark stripe such as giving a curvature to wave front of the soliton leads to vortex interactions and annihilations. We have also developed a method based on the relative phase shift between the fluid and the soliton which is equivalent to an effective time shift. This way, it is possible to observe vortex dynamics without changing any parameter of the nonlinear medium improving the interpretability of the

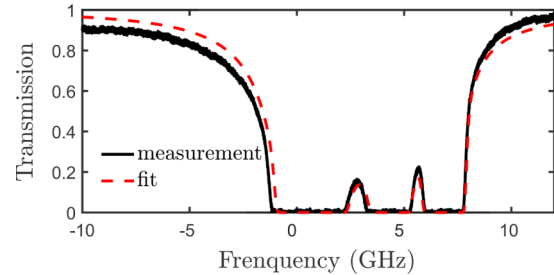


FIG. 6. Transmission of the laser beam through the cell as a function of the detuning  $\delta$  of the laser. From the transmission profile a fit to the data allows us to deduce the temperature of the gas. For this particular curve, we find  $T = 110^\circ\text{C}$ .

results. Numerical simulations have confirmed these results. The techniques developed and tested in this work are scalable to bigger experiments and are aimed to produce and control systems with a greater number of vortices engaged in chaotic interactions of hydrodynamic type. Thus, our work gives additional tools to control and study optical vortex interactions and all phenomena related to it such as fully developed 2D turbulence in optical fluids. An initial density jump like the one in the Josephson junctions setup [14] is another promising setup for creating turbulence in future experiments.

## ACKNOWLEDGMENTS

This work was supported by the EU Horizon 2020 research and innovation programme in the framework of Marie Skłodowska-Curie HALT project (Agreement No. 823937) and the FET Flagships PhoQuS project (Agreement No. 820392). This work also benefited from funding of the project OPTIMAL granted by the European Union by means of the Fond Européen de Développement Régional (FEDER).

## APPENDIX: EVALUATION OF THE TEMPERATURE OF THE ATOMIC VAPOR

To extract atomic gas temperature, we measure the transmission profile of a weak laser beam after propagation through the vapor as a function of the laser detuning. Fitting this data (as shown in Fig. 6) with a numerical simulation taking into account atomic lines of both isotopes, rubidium vapor pressure as a function of the temperature [41–43], and the Doppler broadening, we can deduce the atomic density and therefore link it to the gas temperature using the vapor pressure [44] and ideal gas law.

[1] W. Wan, S. Jia, and J. W. Fleischer, *Nat. Phys.* **3**, 46 (2007).  
 [2] C. Michel, O. Boughdad, M. Albert, P.-É. Larré, and M. Bellec, *Nat. Commun.* **9**, 2108 (2018).  
 [3] D. Vocke, T. Roger, F. Marino, E. M. Wright, I. Carusotto, M. Clerici, and D. Faccio, *Optica* **2**, 484 (2015).  
 [4] D. Vocke, K. Wilson, F. Marino, I. Carusotto, E. M. Wright, T. Roger, B. P. Anderson, P. Öhberg, and D. Faccio, *Phys. Rev. A* **94**, 013849 (2016).

[5] G. A. Swartzlander and C. T. Law, *Phys. Rev. Lett.* **69**, 2503 (1992).  
 [6] V. Tikhonenko, J. Christou, B. Luther-Davies, and Y. S. Kivshar, *Opt. Lett.* **21**, 1129 (1996).  
 [7] N. Šantić, A. Fusaro, S. Salem, J. Garnier, A. Picozzi, and R. Kaiser, *Phys. Rev. Lett.* **120**, 055301 (2018).  
 [8] Q. Fontaine, T. Bienaimé, S. Pigeon, E. Giacobino, A. Bramati, and Q. Glorieux, *Phys. Rev. Lett.* **121**, 183604 (2018).

- [9] Q. Fontaine, P.-E. Larré, G. Lerario, T. Bienaimé, S. Pigeon, D. Faccio, I. Carusotto, E. Giacobino, A. Bramati, and Q. Glorieux, *Phys. Rev. Res.* **2**, 043297 (2020).
- [10] S. Dyachenko, A. Newell, A. Pushkarev, and V. Zakharov, *Physica D* **57**, 96 (1992).
- [11] S. Nazarenko, *Wave Turbulence*, Lecture Notes in Physics, Vol. 825 (Springer-Verlag, Berlin, 2011).
- [12] S. Nazarenko and M. Onorato, *J. Low Temp. Phys.* **146**, 31 (2007).
- [13] S. Nazarenko, M. Onorato, and D. Proment, *Phys. Rev. A* **90**, 013624 (2014).
- [14] A. Griffin, S. Nazarenko, and D. Proment, *J. Phys. A: Math. Theor.* **53**, 175701 (2020).
- [15] M. Abid, C. Huepe, S. Metens, C. Nore, C. T. Pham, L. S. Tuckerman, and M. E. Brachet, *Fluid Dynamics Research* **33**, 509 (2003).
- [16] E. A. L. Henn, J. A. Seman, G. Roati, K. M. F. Magalhaes, and V. S. Bagnato, *Phys. Rev. Lett.* **103**, 045301 (2009).
- [17] U. Bortolozzo, J. Laurie, S. Nazarenko, and S. Residori, *J. Opt. Soc. Am. B* **26**, 2280 (2009).
- [18] J. Laurie, U. Bortolozzo, S. Nazarenko, and S. Residori, *Phys. Rep.* **514**, 121 (2012).
- [19] E. Turitsyna, S. Smirnov, S. Sugavanam *et al.*, *Nat. Photonics* **7**, 783 (2013).
- [20] B. B. Kadomtsev and V. I. Petviashvili, *Sov. Phys. Dokl.*, 15, 539 (1970).
- [21] E. A. Kuznetsov and S. K. Turitsyn, *Zh. Eksp. Teor. Fiz* **94**, 129 (1988) [*JETP* **67**, 1583 (1988)].
- [22] E. A. Kuznetsov and J. J. Rasmussen, *Phys. Rev. E* **51**, 4479 (1995).
- [23] W. Krolikowski and B. Luther-Davies, *Opt. Lett.* **18**, 188 (1993).
- [24] W. Królikowski, X. Yang, B. Luther-Davies, and J. Breslin, *Opt. Commun.* **105**, 219 (1994).
- [25] C. A. Jones and P. H. Roberts, *J. Phys. A: Math. Gen.* **15**, 2599 (1982).
- [26] C. T. Law and G. A. Swartzlander, *Opt. Lett.* **18**, 586 (1993).
- [27] A. Maitre, F. Claude, G. Lerario, S. Koniakhin, S. Pigeon, D. Solnyshkov, G. Malpuech, Q. Glorieux, E. Giacobino, and A. Bramati, *EPL* **134**, 24004 (2021).
- [28] T. Boulier, H. Terças, D. Solnyshkov, Q. Glorieux, E. Giacobino, G. Malpuech, and A. Bramati, *Sci. Rep.* **5**, 9230 (2015).
- [29] G. Verma, U. D. Rapol, and R. Nath, *Phys. Rev. A* **95**, 043618 (2017).
- [30] G. I. Taylor, *Proc. Royal Soc. London Series A* **164**, 476 (1938).
- [31] A. V. Mamaev, M. Saffman, and A. A. Zozulya, *Phys. Rev. Lett.* **76**, 2262 (1996).
- [32] N. Verrier and M. Atlan, *Appl. Opt.* **50**, H136 (2011).
- [33] A. Eloy, O. Boughdad, M. Albert, P. Élie Larré, F. Mortessagne, M. Bellec, and C. Michel, *EPL* **134**, 26001 (2021).
- [34] J.-C. Chanteloup, *Appl. Opt.* **44**, 1559 (2005).
- [35] J. Primot and L. Sogno, *J. Opt. Soc. Am. A* **12**, 2679 (1995).
- [36] S. Velghe, J. Primot, N. Guérineau, M. Cohen, and B. Wattellier, *Opt. Lett.* **30**, 245 (2005).
- [37] P. Azam, A. Fusaro, Q. Fontaine, J. Garnier, A. Bramati, A. Picozzi, R. Kaiser, Q. Glorieux, and T. Bienaimé, *Phys. Rev. A* **104**, 013515 (2021).
- [38] Y. Zhang, X. Cheng, X. Yin, J. Bai, P. Zhao, and Z. Ren, *Opt. Express* **23**, 5468 (2015).
- [39] W. Kwon, G. Del Pace, K. Khani, L. Galantucci, A. Muzi Falconi, M. Inguscio, F. Scazza, and G. Roati, *Nature (London)* **600**, 64 (2021).
- [40] See Supplemental Material at <http://link.aps.org/supplemental/10.1103/PhysRevA.105.043510> for video.
- [41] P. Siddons, C. S. Adams, C. Ge, and I. G. Hughes, *J. Phys. B: At., Mol. Opt. Phys.* **41**, 155004 (2008).
- [42] I. H. Agha, C. Giarmatzi, Q. Glorieux, T. Coudreau, P. Grangier, and G. Messin, *New J. Phys.* **13**, 043030 (2011).
- [43] Q. Baudouin, R. Pierrat, A. Eloy, E. J. Nunes-Pereira, P.-A. Cuniasse, N. Mercadier, and R. Kaiser, *Phys. Rev. E* **90**, 052114 (2014).
- [44] D. A. Steck, <https://steck.us/alkalidata/rubidium87numbers.pdf>.